

The Advanced Camera for the Hubble Space Telescope

Holland Ford^a, Frank Bartko^a, Pierre Bely^a, Thomas Broadhurst^a, Chris Burrows^a, Edward Cheng^a, Mark Clampin^a, Jim Crocker^a, Paul Feldman^a, David Golimowski^a, George Hartig^a, Garth Illingworth^a, Randy Kimble^a, Michael Lesser^a, George Miley^a, Susan Neff^a, Marc Postman^a, William Sparks^a, Zlatan Tsvetanov^a, and Rick White^a; Pamela Sullivan^b, Carolyn Krebs^b, and Douglas Leviton^b; Tom LaJeunesse^c, Bill Burmester^c, Sherri Fike^c, Rich Johnson^c, Bob Slusher^c, Paul Volmer^c, and Bob Woodruff^c

^a. ACS Science and Engineering Instrument Definition Team

^b. Goddard Space Flight Center Management and Engineering Team

^c. Ball Aerospace Management and Engineering Team

ABSTRACT

The *Advanced* Camera for the Hubble Space Telescope has three cameras. The first, the Wide Field Camera, will be a high-throughput (44% at 600 nm, including the HST OTA), wide field (200"×204"), 4096 × 4096 pixel CCD optical and I-band camera that is half-critically sampled at 500 nm. The second, the High Resolution Camera (HRC), is a 1024 × 1024 pixel CCD camera that is critically sampled at 500 nm. The HRC has a 26"×29" field of view and 29% throughput at 250 nm. The HRC optical path includes a coronagraph that will improve the HST contrast near bright objects by a factor of ~10 at 900 nm. The third camera, the Solar-Blind Camera, is a far-ultraviolet, pulse-counting array that has a relatively high throughput (6% at 121.6 nm) over a 26"×29" field of view. The Advanced Camera for Surveys (ACS) will increase HST's capability for surveys and discovery by a factor of ~10 at 800 nm.

The ACS science team will use ~60% of its dedicated time to make deep surveys of 15 clusters of galaxies at redshifts between 0.2 and 2. We will map the large-scale distribution of dark matter around two low redshift rich clusters and investigate the evolution of galaxies and clusters of galaxies between redshifts of 0.5 and 1. We will study young galaxies and clusters of galaxies in fields centered on high-redshift radio galaxies. HRC images of an unbiased sample of early-type galaxies will be searched for small ($r \sim 100$ pc) nuclear disks; subsequent spectroscopic observations of the disks will be used to measure the central masses to determine if massive black holes are present. We will use the HRC coronagraph to take broad-band, narrow-band, and polarimetric images of quasars and BL Lacs at redshifts between 0.2 and 0.5. We will use a novel polarimetric technique to measure geometric distances to galaxies and provide independent measures of H_0 . The coronagraph will be used to search nearby stars for proto-planetary disks, brown dwarf companions, and planets.

1. OVERVIEW OF THE ADVANCED CAMERA

The design of the Hubble Space Telescope (HST) Advanced Camera for Surveys (ACS) and the philosophy underlying the design has been described in detail by Ford *et al.* (1996). At this time (March 1998) the instrument design is complete, nearly all of the mechanisms have been built, sub-systems such as electronics and the cameras are being built, and integration of the ACS has begun. The series of papers in this volume written by the ACS science and engineering team document the status of the instrument in early 1998. Woodruff and Cahill (1998) describe the ACS optical design, and Clampin *et al.* (1998) present the performance of the ACS CCDs measured before integration into their vacuum enclosures. The papers by Rafal (1998) and by Schweickart and Johnson (1998) describe the ACS thermal design, the HST Aft Shroud Cooling System, and the design and performance of the ACS flexible heat pipes. Tsvetanov *et al.* (1998), Leviton *et al.* (1998a,b), and Boucarut and Leviton (1998) document the calibration and measured characteristics of the ACS filters. Fike and Schoeneweis (1998) describe the plan for integrating and testing ACS flight software. Hartig *et al.* (1998) present the ACS calibration and performance verification plan. The novel approach to the program management of the ACS program is discussed by Krebs *et al.* (1998).

In this paper we concentrate on the measured characteristics of the optics and detectors and the ACS performance predicted from these measurements. The ACS will be thoroughly tested and calibrated in the fall of 1998 after integration and assembly is completed. In a future paper we will publish the ACS system performance measured during thermal-vacuum testing at Ball Aerospace.

The ACS has three cameras. The first, the Wide Field Camera (WFC), will be a high-throughput (44% at 600 nm, including the HST OTA), wide field (200'' × 204''), 4096 × 4096 pixel CCD optical and I-band camera that is half-critically sampled at 500 nm. The second, the High Resolution Camera (HRC), is a 1024 × 1024 pixel CCD camera that is critically sampled at 500 nm. The HRC has a 26'' × 29'' field of view and high sensitivity in the near ultraviolet (29% at 250 nm, including the OTA). The HRC optical path includes a coronagraph that will improve the HST contrast near bright objects by a factor of ~10. The third camera, the Solar-Blind Camera, is a far-ultraviolet, pulse-counting array that has a relatively high throughput (6% at 121.6 nm) over a 26'' × 29'' field of view. The positions of the three cameras, filter wheels, and shutters within the ACS optical bench are shown in Figure 1.

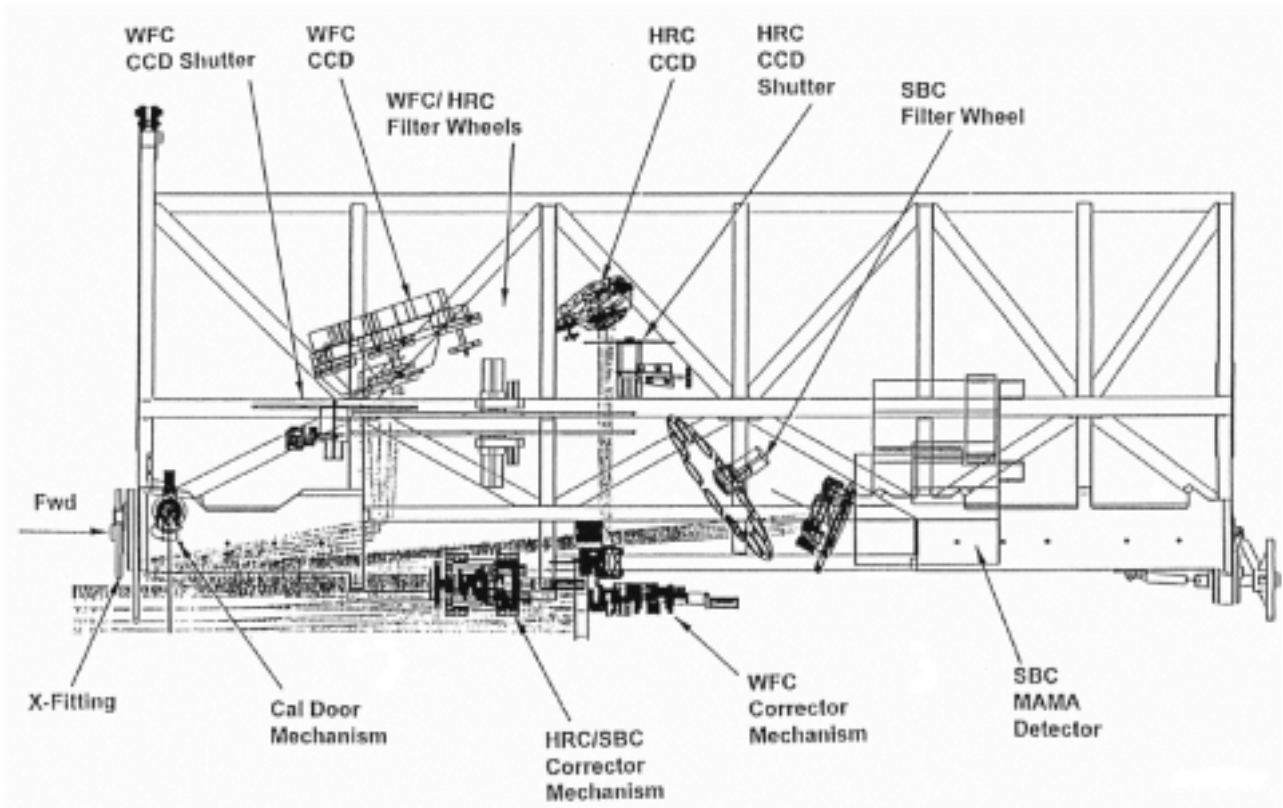


Fig. 1: The layout of the ACS optical bench.

The key characteristics of the ACS are listed in Table 1. The throughputs include the geometrical, scattering, and reflectivity losses from the HST optical telescope assembly (Burrows, 1990). The WFC efficiencies are based on the quantum efficiencies (QEs) of the Scientific Imaging Technologies (SITE) 2k × 4k WFC CCDs selected for the second build of the WFC thermal enclosures. The HRC efficiency is derived from the measured QE of the SITE 1k × 1k CCD chosen for build two of the flight HRC.

For comparison, Table 1 includes the WFPC2 (Burrows et al. 1995) and STIS (Baum et al. 1996), two cameras that will be in the HST after the ACS is installed during the third HST servicing mission in late 1999 or early in 2000. The ACS will provide large gains in sensitivity and field of view compared to the WFPC2. The product of the QE and the field of view (the discovery efficiency) is a measure of how efficiently a camera can be used for surveys. The near-infrared bandpass centered on 800 nm is particularly important for surveys to find galaxies at high redshift. The ACS will have a discovery efficiency that is ~10 times better than the WFPC2 in the I-band. The WFC will have twice the resolution of the WFPC2, and the HRC, which fully samples the HST point spread function at wavelengths $\lambda \geq 500$ nm, will have twice the resolution of the PC2 camera and STIS.

Table 1: Key Characteristics of the Advanced Camera for Surveys

Prioritized Features	WFC		HRC		SBC	
	ACS WFC	WFPC2 f/12.9	ACS HRC	WFPC2 f/17.9	ACS SBC	STIS SBC
Maximum Throughput including HST OTA (%)	44 @ 600 nm	14.5@600 nm	29@250 nm	14.5@600 nm	6.0@125.4 nm	5@125.4 nm
at 800 nm	34	7.0	16	7.0	5.8 @121.6	4.3 @121.6
at 400 nm	30	5.7	25	5.7	5.7 @135.4	3.8 @135.4
at 250 nm	---	3.0	29	3.0	4.9 @140.3	3.4 @ 140.3
					3.8 @148.7	2.3 @ 148.7
					2.3 @160.8	1.2 @ 160.8
Equiv. FOV	200" × 204"	143" × 143"	26" × 29"	35" × 3 5"	26" × 29"	50" × 50"
Sampling @ 500 nm	Half	Quarter	Full	Half	Half***	Half
Polarization from design and coating	<1%	~5%	<5%	~5%	<1%	

*** 632.8@ nm

2. INSTRUMENT DESIGN

The light path through the ACS to the WFC is shown schematically in Figure 2. The light first encounters the spherical mirror IM1 which images the HST pupil onto the IM2 mirror. The IM2 mirror is an anamorphic asphere that is figured with the inverse conic error on the HST primary mirror. IM2 corrects the spherical aberration in the HST primary and the field dependent astigmatism of the HST at the center of the ACS field of view. The light from the IM2 mirror is reflected by IM3, a Schmidt-like plate, through the two filter wheels to the WFC CCDs. The Schmidt plate corrects astigmatism over the WFC field of view (FOV). The WFC has two side-by-side Scientific Imaging Technologies (SITe) 2048 × 4096 CCDs with 15 micron pixels. The gap between the two CCDs is approximately 20 pixels. The WFC and HRC CCDs are described in detail by Clampin *et al.* (1998) in this volume. The f/25 focal length of the WFC gives 0.051 "/pixel and near critical sampling in the I-band.

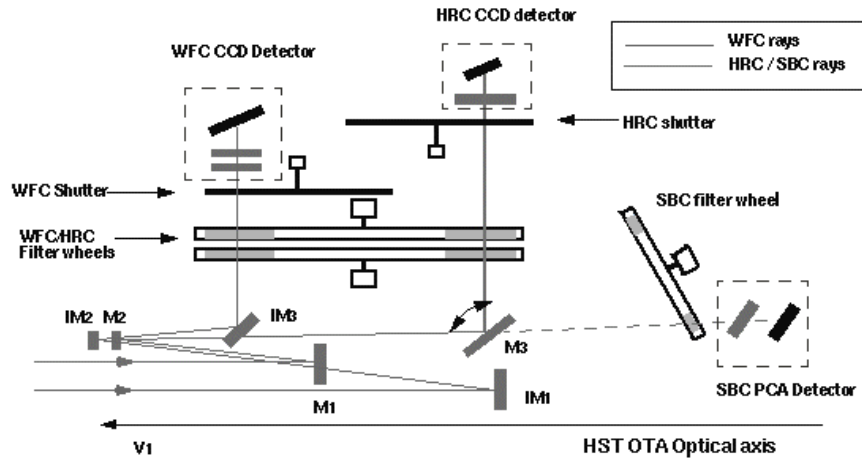


Fig. 2: An optical schematic of the Advanced Camera

3. THE WIDE FIELD CAMERA

The WFC was designed to maximize the instrument throughput at 800 nm. To achieve this goal, each of the three WFC mirrors has a Denton protected-silver coating. Figure 3 shows the average of the reflectivity measured by Ball on four IM2 and four IM3 witness mirrors. The angle of incidence onto IM3 is approximately 45°. The reflectivity measured by Denton on an IM3 witness mirror at $i = 45^\circ$ and the reflectivity measured by Ball at normal incidence are, to within the measurement errors, the same at wavelengths > 400 nm. The reflectivity of three silver-coated mirrors is 50 percent higher than three aluminum-coated mirrors at 800 nm. Overcoated silver mirrors maintain high reflectivity for several years with exposure to typical laboratory air quality and humidity.

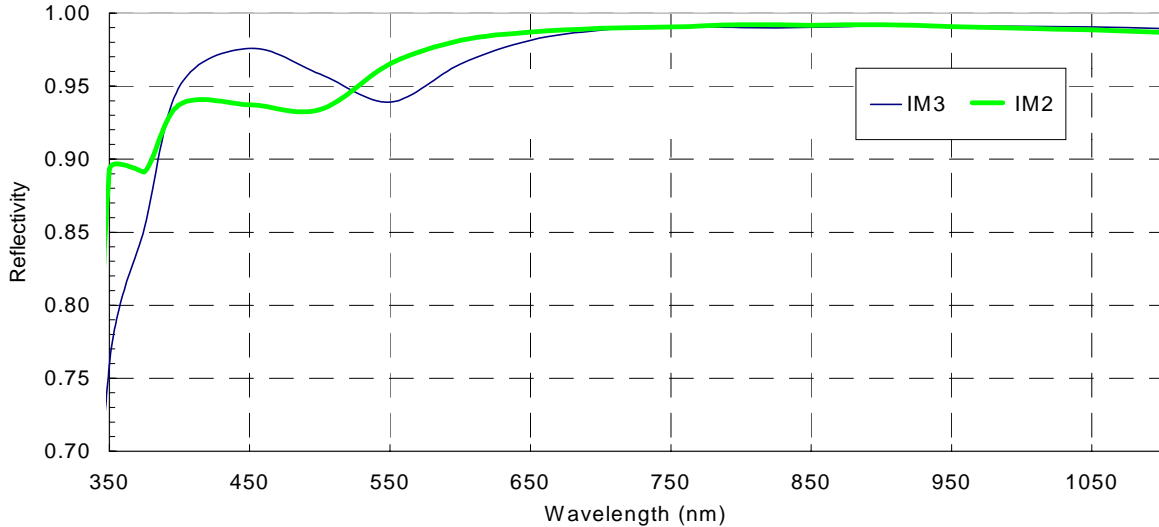


Fig. 3: Average reflectivity of the IM2 and IM3 witness mirrors

The two WFC CCDs are mounted in a vacuum enclosure that is designed to isolate the CCDs from thermal radiation and contamination. Figure 4 shows a schematic of the enclosure. The enclosure is connected by two passive heat pipes to an interface plate on the ACS enclosure. One set of heat pipes connects the interface plate to an ACS radiator panel, which radiates heat into the aft shroud. A second pair of heat pipes connects the interface plate to a radiator that is on the outside of the HST. The design of the Swales heat pipes is discussed by Schweickart and Johnson (1998) in this volume. The Aft Shroud Cooling System and ACS thermal design are discussed by Rafal (1998) in this volume. Each thinned WFC CCD is bonded to a soda glass die. The die is in turn bonded with indium solder to an AlN CCD carrier. Two CCD carriers are in turn soldered side by side to another AlN plate, the focal plane carrier. Finally, the focal plane carrier is attached to a single four-stage TEC. The entire assembly is enclosed in an evacuated housing which has been cleaned and baked at high temperature before sealing. The enclosure has an anti-reflection, coated fused-silica window at ambient temperature.

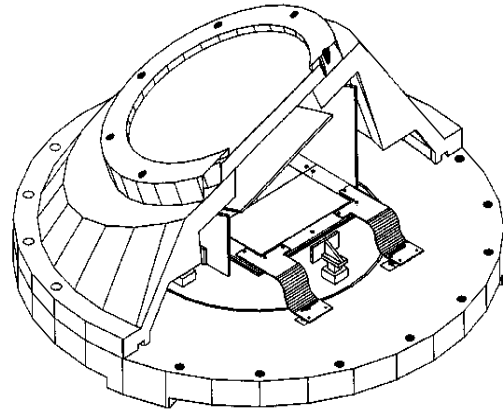


Fig. 4: Schematic of the WFC CCD housing

The heat load on the large WFC CCD is reduced by a cooled inner enclosure and a second cooled anti-reflection coated fused-silica window. The innermost enclosure is cooled by four two-stage TECs. We expect the CCDs to operate between -80°C to -85°C , depending on the interior and exterior thermal loads on the HST. Figure 5 shows the high transmission measured for one of the two WFC windows. The QEs of the CCDs selected for Flight Build 2 are shown in Figure 6.

Table 2 lists the charge transfer efficiency (CTE), dark current, rms read noise, the fraction of pixels with less than 80% of the peak QE (i.e., the number of “cool-pixels”), and the full well for the CCDs in Flight Build 2. The WFC1 CCD has a relatively large fraction (~2%) of cool-pixels because a transparent film of gold was inadvertently deposited onto one corner and along the edges during processing. We expect that “flat-fielding” will remove the uniform shading in the areas of gold deposition.

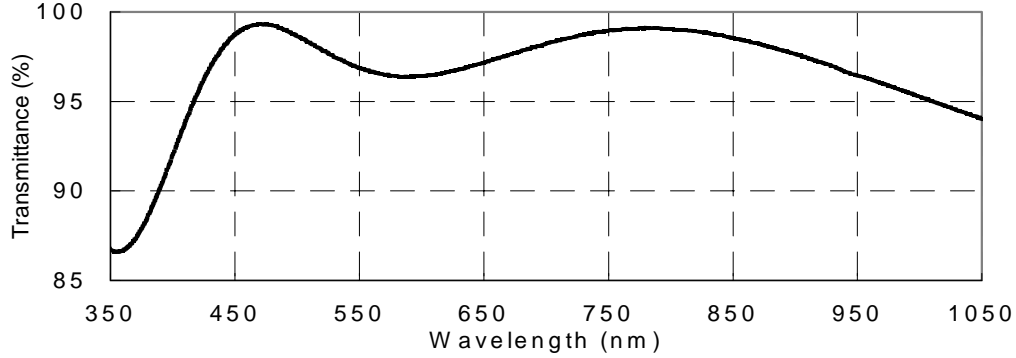


Fig. 5: The measured transmission versus wavelength for one of the two WFC windows coated by REO.

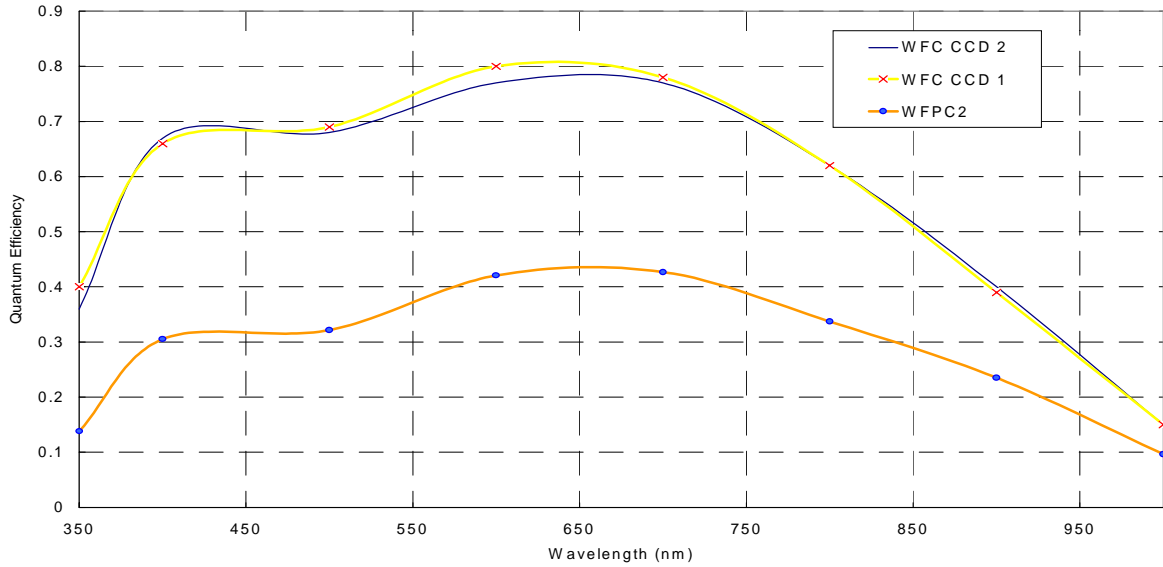


Fig. 6: The quantum efficiencies of the two CCDs in the WFC Flight Build 2. The QE of the WFPC2 is included for comparison.

Table 2: Characteristics of the Flight Build 2 CCDs

	WFC1 (5412MBR0301)	WFC2 (5412MBR1301)
Parallel CTE, A Amp	0.999949	0.999989
Parallel CTE, B Amp	0.999961	0.999985
Serial CTE, A Amp	0.999995	0.999996
Serial CTE, B Amp	0.999998	0.999995
Dark Current @ -80° C (e/pixel/hour)	11	8
RMS Read Noise, A Amp (electrons)	5.3	8.4
RMS Read Noise, B Amp (electrons)	5.0	5.9
Cool-Pixel Fraction (%)	2	0.1
Full Well (electrons)	80,000	80,000

The expected performance of the HST + WFPC as a function of wavelength is shown in Figure 7 and listed in Table 3. The net efficiency derived from the product of the HST and OTA has been multiplied by the "loss factor" 0.95 to allow for up to 1% loss at each WFC optical element from the accumulation of dust and contaminants before launch. We have included the net efficiency of the WFPC2 and STIS for comparison.

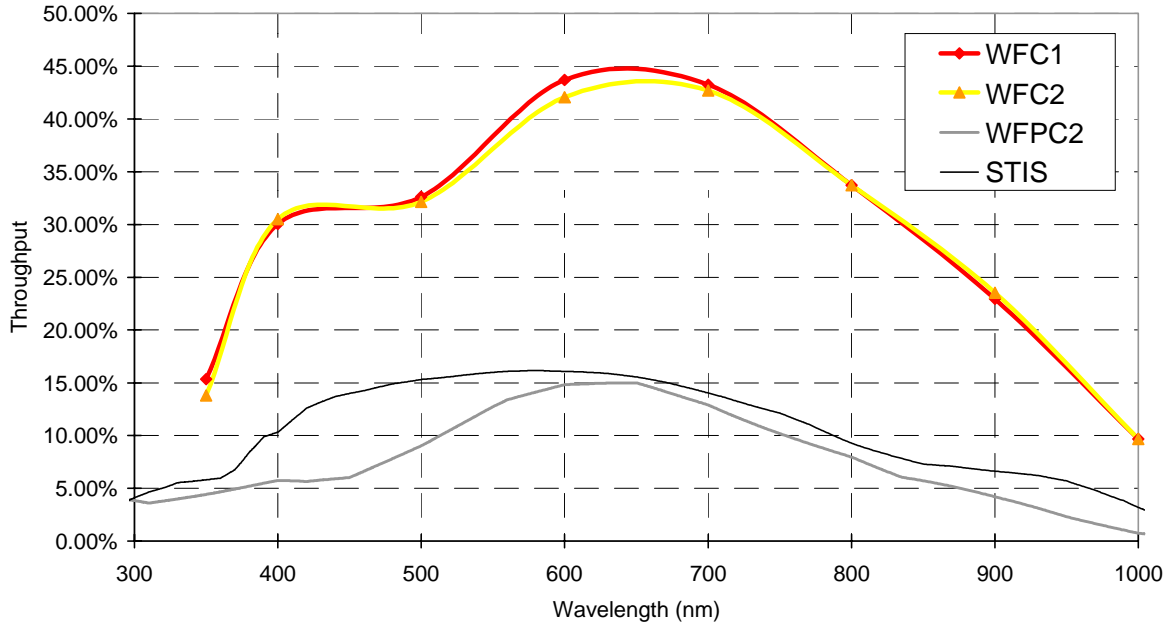


Fig. 7: The expected net throughput for the HST + WFC. The WFPC2 and STIS are shown for comparison.

Table 3: The Expected Net Efficiency for the Flight Build 2 WFC

wavelength (nm)	OTA	IM2	IM3	Ext-Win	Int-Win	Loss Factor	WFC1 QE	WFC2 QE	WFC1 Net Eff	WFC1 Net Eff
350	0.621	0.892	0.386	0.954	0.958	0.95	0.36	0.40	0.14	0.15
400	0.636	0.937	0.950	0.952	0.962	0.95	0.67	0.66	0.31	0.30
500	0.640	0.934	0.958	0.974	0.980	0.95	0.68	0.69	0.32	0.33
600	0.636	0.981	0.965	0.977	0.979	0.95	0.77	0.80	0.42	0.44
700	0.621	0.990	0.988	0.984	0.986	0.95	0.77	0.78	0.43	0.43
800	0.605	0.992	0.990	0.984	0.985	0.95	0.62	0.62	0.34	0.34
900	0.640	0.992	0.991	0.996	0.995	0.95	0.40	0.39	0.24	0.23
1000	0.716	0.990	0.991	0.989	0.988	0.95	0.15	0.15	0.10	0.10

4. THE HIGH RESOLUTION CAMERA

The HRC detector is a SITE 1024×1024 CCD with 21μ pixels. The $f/70$ optics give an angular scale of $0.25''/\text{pixel}$, a $26'' \times 29''$ FOV, and critical sampling at wavelengths longer than 500 nm. The HRC CCD is mounted in a vacuum enclosure which is a STIS mechanical and thermal design. The single fused-silica CCD detector window is oriented normal to the chief ray to minimize lateral color. The CCD is tilted to match the best image surface. The angle between the window and the CCD is 30.8 degrees.

The HRC and the SBC use the same M1 and M2 mirrors, as shown in Figure 2. The resultant image quality at the CCD surface is equal to or better than $\lambda/20$ everywhere. Residual aberrations are balanced to yield an optimum image over the HRC and the SBC FOV. The design wavefront error varies from 0.003 to 0.018 waves rms at 632.8 nm over the field. When this nominal design value is error-budgeted with other expected wavefront errors due to manufacture, CCD curvature, and alignment, the overall wavefront error is estimated to be less than 0.065 waves at 632.8 nm, which yields a high Strehl ratio of 82 percent.

The MgF₂ overcoatings on these two aluminum-coated mirrors are optimized for maximum reflectivity at 121.6 nm. Because of reflection losses in the far ultraviolet, we chose to have only two reflections in the optical path to the SBC. A flat mirror M3 is inserted into the light path to direct the light through the two filter wheels to the HRC CCD. The MgF₂ coating on this mirror is optimized for maximum reflectivity at wavelengths longer than 200 nm. The first two mirrors are used at near normal incidence to minimize the polarization sensitivity. Including the fold mirror, which is used at a 47.9 degree angle of incidence, this configuration yields only 1.0 percent degree of polarization sensitivity at 436 nm and 4.3 percent at the worst case wavelength of 800 nm.

The reflectivities of the M1, M2 and M3 mirrors are plotted in Figure 8. The transmission of the AR-coated fused-silica window is shown in Figure 9.

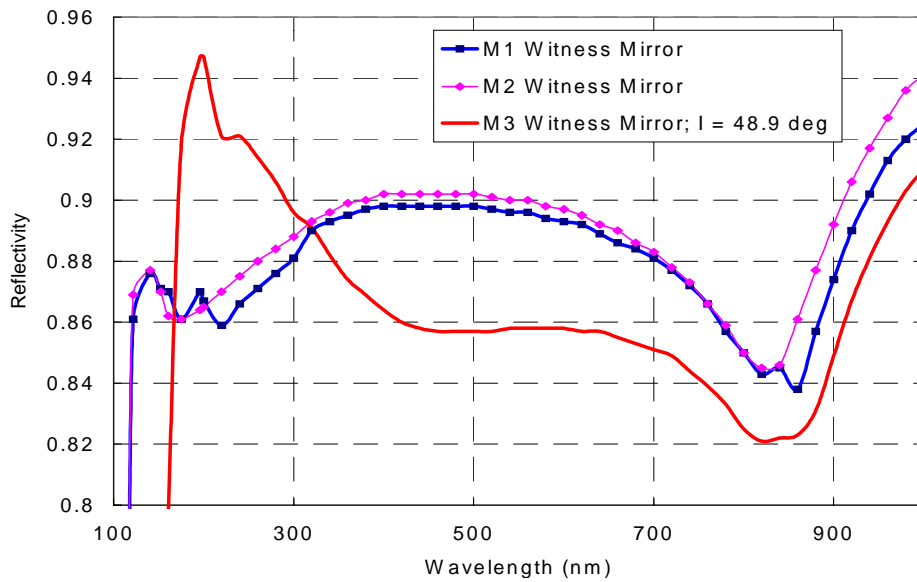


Fig. 8: The measured reflectivities of the M1, M2, and M3 mirrors.

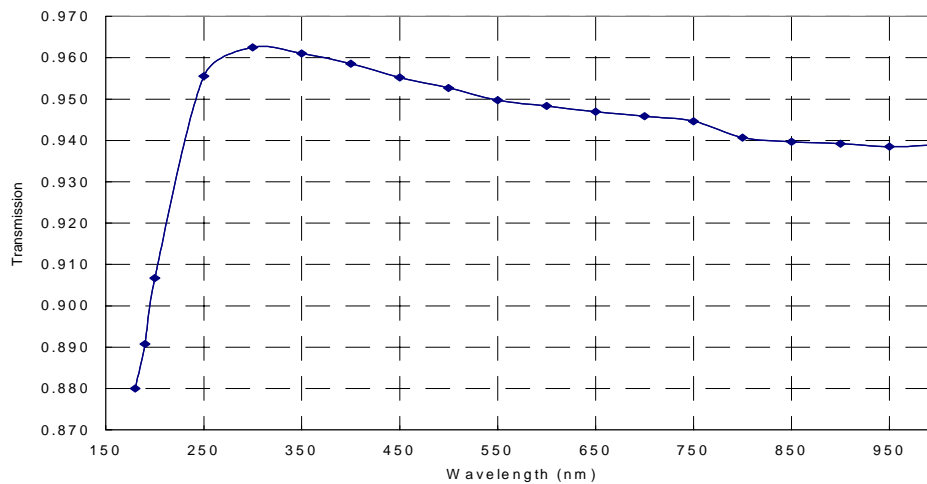


Fig. 9: The transmission of the AR-coated fused-silica window in the HRC thermal enclosure.

The HRC CCD in Flight Build 1 has the QE shown in Figure 10. This CCD has SITE's new "UVIS" coating that has higher QE in the near-UV than the SITE coating used on the STIS $1k \times 1k$ CCD. The characteristics of the Build 1 CCD, which has excellent cosmetics and readnoise, are listed in Table 4. The readnoise and full well were measured by SITE; all other measurements were made by Ball. The CTE was measured by exposing the CCD to Fe 55 X-rays. Each detected X-ray produces 1620 electron-hole pairs.

Table 4: Characteristics of the HRC Build 1 and Build 2 CCDs

	Build 1 (7161LXD01-02)			Build 2 (7282LDN01-02)		
	Parallel CTE	Serial CTE	Read Noise	Parallel CTE	Serial CTE	Read Noise
A amp (e)	0.99998	0.999992	3	0.99999	0.999995	< 5.6
B amp (e)	0.99998	0.999990	3	0.99999	0.999997	< 5.2
C amp (e)	0.99999	0.999998	2.7	0.99999	0.999992	< 5.1
D amp (e)	0.99998	0.999996	2.6	0.99999	0.999994	< 5.8
Dark Current (e/pix/hour)	~18			~20		
Full Well (e)	~150,000			~150,000		

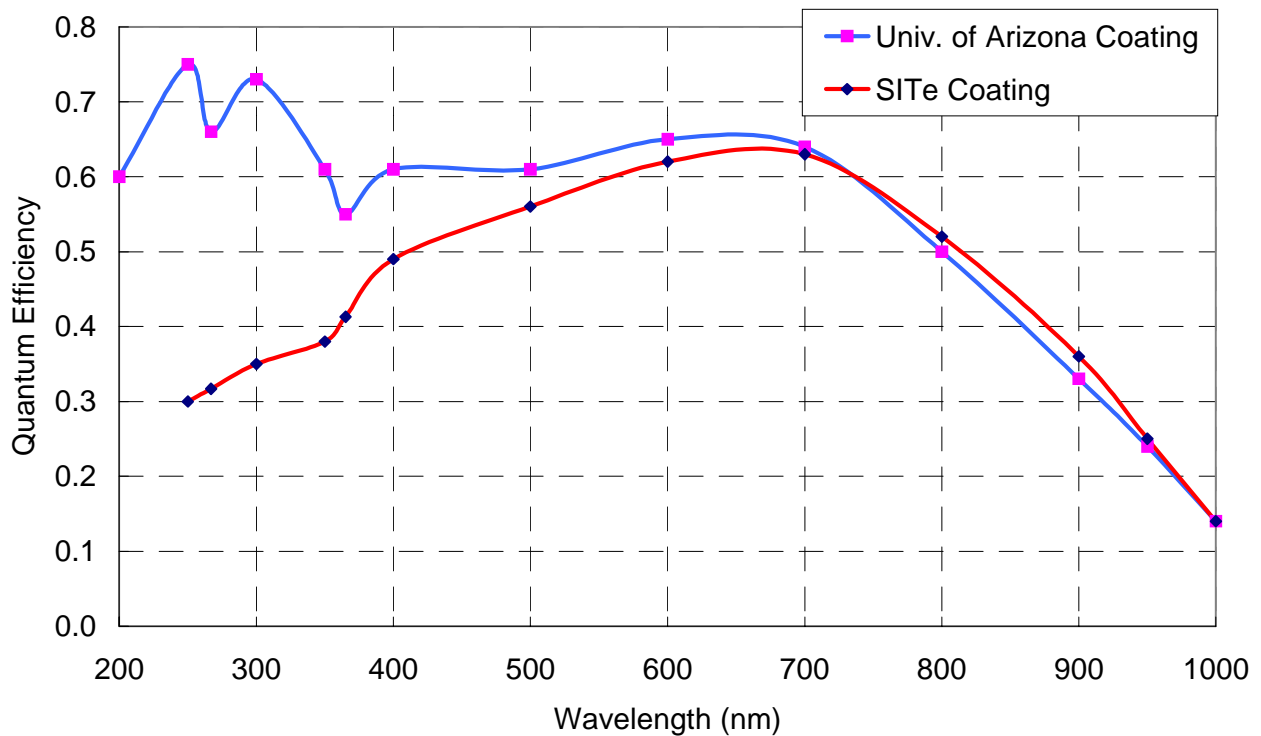


Fig. 10: The quantum efficiencies of the HRC Build 2 CCD (Lesser coating) and the Build 1 CCD (SITE UVIS coating).

Flight Build 2 has a SITE $1k \times 1k$ CCD with a coating provided by Mike Lesser at the University of Arizona. The high QE of this device in the near ultraviolet is shown in Figure 10. At this time we plan to use Build 2 in the ACS. Because of system noise in the Ball test facility, the rms readnoise shown for the Build 2 CCD is an upper limit to the intrinsic read noise, which we expect to be ~ 3 rms electrons per pixel.

The estimated net efficiency of the HST OTA+HRC is shown in Figure 11 and listed in Table 5. The ACS F250W filter has approximately 3 times the transmission of the WFPC2 F250W filter. When this filter is used, the HRC with Flight Build 2 is approximately 20 times more sensitive than WFPC2.

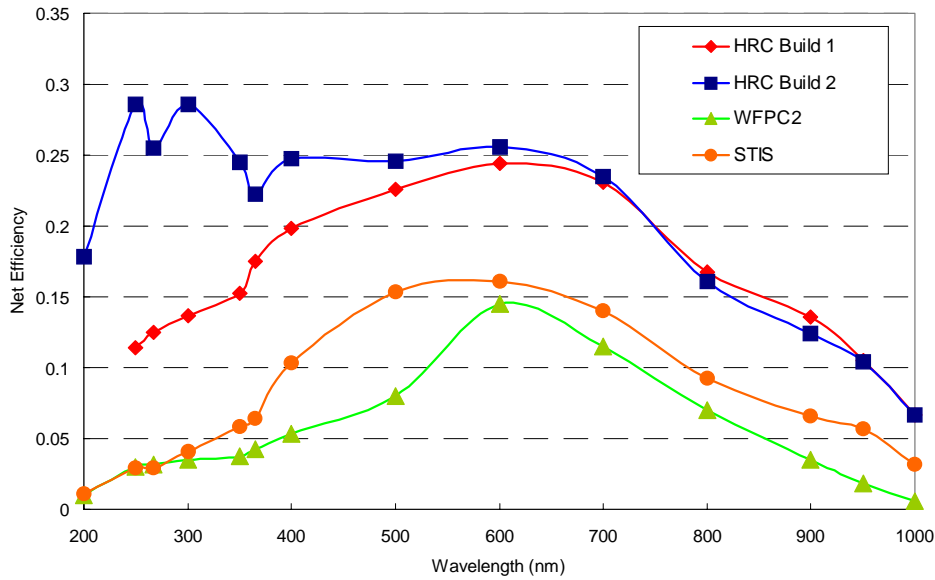


Figure 11: The estimated net efficiency of the HST OTA+HRC with HRC Flight Builds 1 and 2. The WFPC2 and STIS are for comparison.

Table 5: The Expected Net Efficiency for the HRC Flight Builds 1 and 2

λ (nm)	OTA	M1	M2	M3	Window	Loss Factor	HRC Bld 1 QE	HRC Bld 2 QE	Bld 1 Net Eff	Bld 2 Net Eff
200	0.49	0.867	0.865	0.947	0.907	0.95				
250	0.60	0.869	0.878	0.918	0.956	0.95	0.30	0.75	0.11	0.29
300	0.61	0.881	0.888	0.896	0.963	0.95	0.35	0.66	0.14	0.29
350	0.62	0.894	0.898	0.878	0.961	0.95	0.38	0.61	0.15	0.24
400	0.64	0.898	0.902	0.864	0.959	0.95	0.49	0.61	0.20	0.25
500	0.64	0.898	0.902	0.857	0.953	0.95	0.56	0.61	0.23	0.25
600	0.64	0.893	0.897	0.858	0.948	0.95	0.62	0.65	0.24	0.26
700	0.62	0.881	0.883	0.851	0.946	0.95	0.63	0.64	0.23	0.23
800	0.60	0.850	0.850	0.825	0.941	0.95	0.52	0.50	0.17	0.16
900	0.64	0.874	0.892	0.849	0.939	0.95	0.36	0.33	0.14	0.12
1000	0.67	0.925	0.941	0.910	0.939	0.95	0.14	0.14	0.07	0.07

5. THE SOLAR BLIND CAMERA

The ACS solar blind camera is the STIS band 1 flight spare (MAMA 006) generously given to the ACS program by the STIS principal investigator, Dr. Bruce Woodgate, and the HST Project at the Goddard Space Flight Center. Figure 12 shows a picture of the SBC.

The SBC uses a STIS-based PCA photon-counting detector with an opaque CsI photocathode and a C-plate micro-channel plate (MCP). The SBC was optimized for highest throughput from 115 nm to 170 nm by designing the optical path with only two reflections (c.f. Fig. 2). The coatings on the M1 and M2 mirrors, shown in Figure 8, were designed to maximize the reflectivity at 121.6 nm.

The SBC image is sampled at 0.030"/pixel. A full 26" by 29" FOV is available. The SBC image quality is discussed by Woodruff and Cahill (1998) in this volume.

The net efficiency of the SBC, including the HST OTA, is shown in Figure 13. Although the ACS SBC has somewhat higher sensitivity than STIS, the primary advantage of the ACS relative to STIS is a better selection of filters (c.f. Tsvetanov et al., 1998 in this volume). Table 6 lists the important characteristics of the SBC.

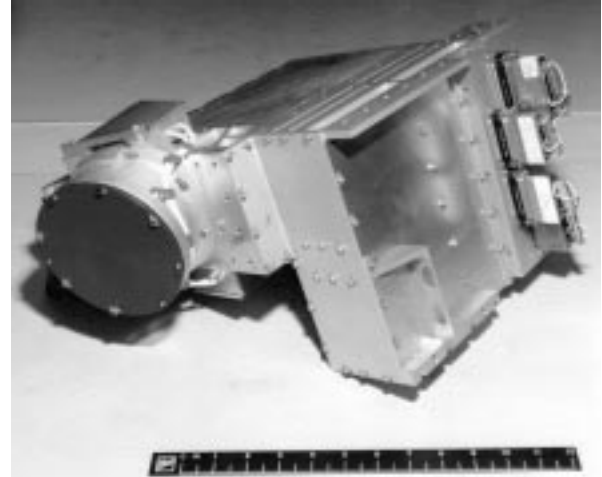


Fig. 12: A picture of the Solar Blind Photon Counting Array Detector. The SBC window is covered with a protective aluminum plate in the picture.

Table 6. Performance Characteristics of the Advanced Camera SBC Detector

Quantity	Value	Wavelength	DQE
Wavelength Range	112 nm – 119 nm	121.6	0.192
Spatial Resolution (FWHM)	28.2 microns	125.4	0.189
Dark Count @ 38° C (c/s/pix)	2.5×10^{-4} global	135.4	0.177
Dark Count @ 38° C (c/s/pix)	6.9×10^{-4} peak	140.3	0.154
Flat Field Uniformity	± 6.2 % rms (1σ)	148.7	0.125
Visible Light DQE		$\lambda > 400$ nm	$< 1.16 \times 10^{-9}$
Broken Electrodes	1		
Bright Spots > 1 c/s	2		
Dark Spots	3		
Spatial Non-Linearity	5 μ /mm (maximum)		
Local Dynamic Range	350 c/pix/s		
Global Dynamic Range	3.6×10^5 c/s		

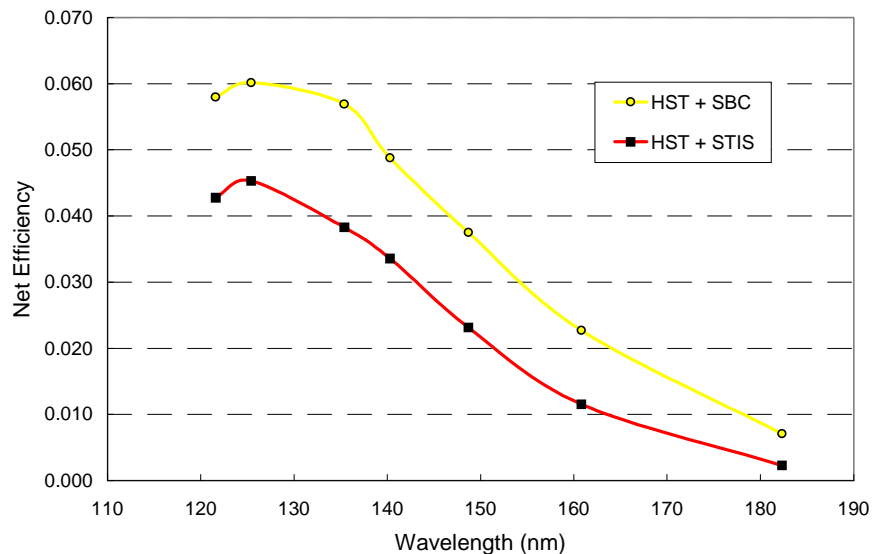


Fig. 13: The HST + SBC net efficiency versus wavelength. The STIS net efficiency is shown for comparison.

6. FILTERS AND DISPERSERS

The complement of ACS filters and dispersers, described by Ford *et al.* (1996) and by Tsvetanov *et al.* (1998) in this volume, is shown schematically below in Figure 14.

Here we call attention to several noteworthy features of the ACS filter set. First, the ACS includes the ‘‘Sloan’’ g, r, i, and z filters. Inclusion of these filters will allow easy transformation of ACS observations into the photometric system of the Sloan Digital Sky Survey.

The ‘‘Narrow Ramps’’ are narrow band filters with a $\sim 2\%$ FWHM bandpass and a central wavelength that varies continuously in one direction. Figure 15 shows a picture of three of the ramp filters in a cell that mounts into the WFC/HRC filter wheels. The central ramp in each cell can be used with the HRC. Each ramp filter is three separate pieces of glass.



Fig. 15: A picture of three ‘‘ramp filters’’ in a filter cell that mounts into the filter wheel.

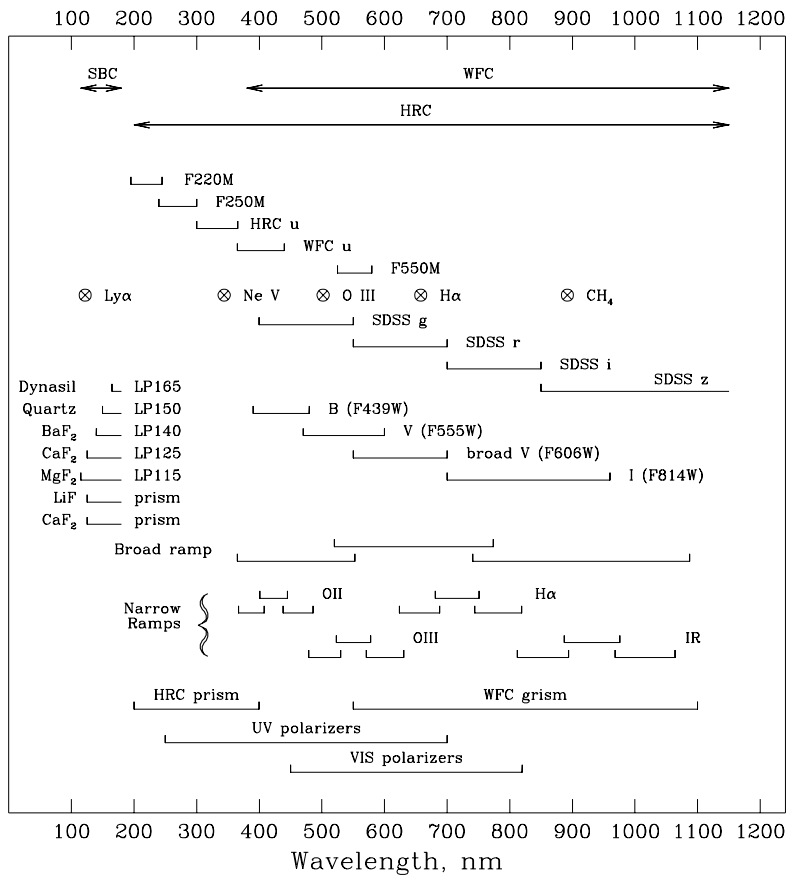


Fig. 14: A schematic showing the ACS filters and dispersers. The wavelength range covered by each camera is shown at the top of the figure. The name of each filter is adjacent to a horizontal bar that shows the filter’s bandpass. The narrow band ($\Delta\lambda/\lambda \cong 1\%$ at FWHM) filters are marked with the symbol ‘‘ \otimes ’’, followed by the name of the emission line the filter transmits. The filters with names in parentheses correspond to the WFPC2 broadband filters, and provide photometric continuity with that instrument. The ‘‘narrow and broad ramps’’ are continuously variable narrow band interference filters that respectively have FWHM bandpasses of $\sim 2\%$ and $\sim 9\%$. The dispersers for low resolution ($\lambda/\Delta\lambda \sim 100$), slitless spectroscopy are two prisms for the SBC, a prism for the HRC, and a grism for the WFC.

In the ACS design the central wavelength of the ramp filters varies along a chord that is perpendicular to the radius of the wheel. The central wavelength is chosen by a combination of target positioning and rotation of the filter wheel. The FWHM field of view at a chosen wavelength is $\sim 50'' \times 70''$ for the WFC. When the ramp filters are used with the HRC the field of view covers almost the entire HRC CCD. Figure 16 shows the field of view of a ramp filter illuminated by monochromatic light.

Another noteworthy feature of the ACS filters is the high transmission of the HRC UV filters relative to previous HST UV filters. Figure 17 shows the transmission of the HRC F220W, F250W, and F330W filters. The corresponding filters for the WFPC2 are shown for comparison. The ACS F220W and F250W respectively transmit approximately 1.5 and 3 times as much light as the WFPC2 F218W and F255W filters, while maintaining excellent out-of-band blocking. The ACS F330W has approximately the same transmission as the WFPC2 F336W, but has much better out-of-band blocking in the red. The high transmission of the filters combined with the high sensitivity of the HRC Build 2 CCD will give efficiency gains of ~ 20 (F220W), ~ 30 (F250W), and 7 (F330W) relative to WFPC2.

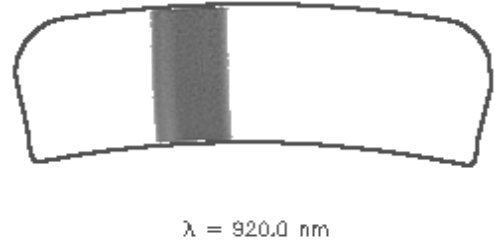


Fig. 16: A picture of a ramp filter illuminated by monochromatic light. As the wavelength of the monochromatic source is varied, the illuminated area moves across the filter.

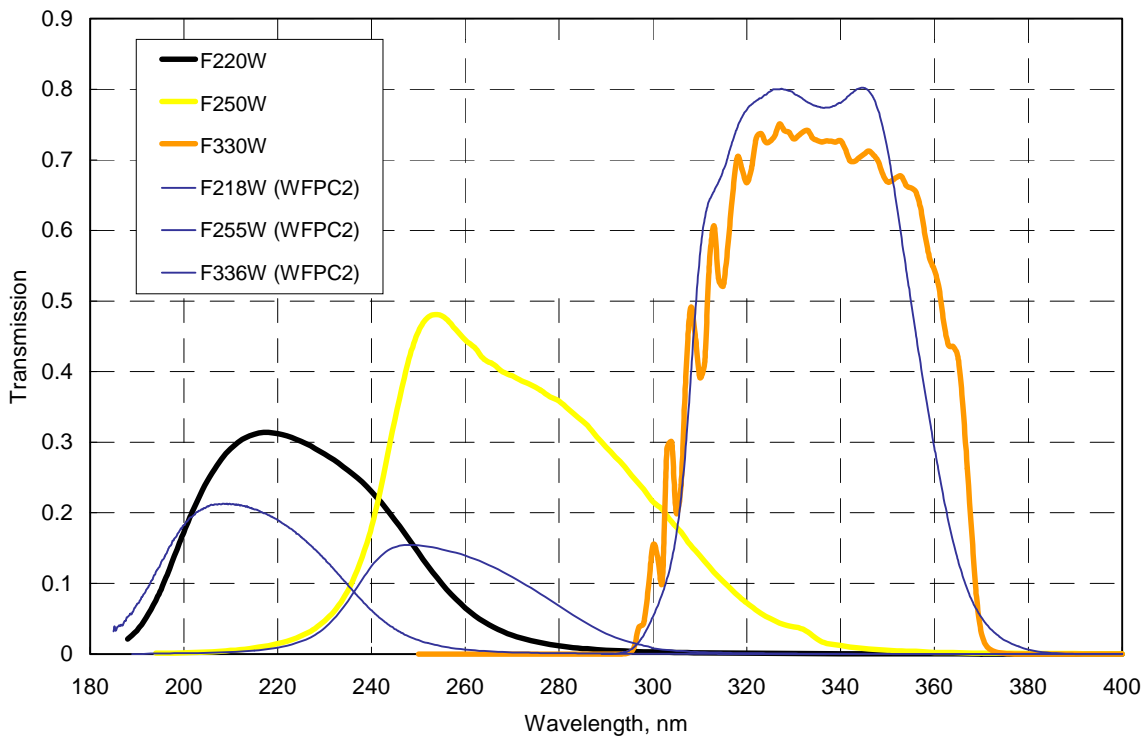


Fig. 17: The transmission of the HRC near UV filters. The corresponding WFPC2 filters are shown for comparison.

7. CORONAGRAPH

The ACS coronagraph will have two high-contrast options. Both options suppress the light from a bright object which is positioned behind a mask using autonomous on-board target acquisition. The first option is a “Fastie spot”, which is a $0.8''$ diameter reflecting spot deposited near the corner of the HRC CCD entrance window (where the beam size is $0.5''$). The Fastie spot enables unvignetted, high-contrast imaging from $0.7''$ to $4''$ around a bright source (for example imaging of a quasar host galaxy) using any of the HRC filters. Vignetted, but still useful data will be available to within $0.4''$ from the

bright source. The Fastie spot does not significantly reduce the level of diffracted light in the wings of a bright point source positioned behind it. However, by preventing the light from crossing the window and hitting the CCD, instrumental scatter, ghosts, and CCD bleeding will be minimized. These effects raise the PSF wings by almost an order of magnitude in WFPC2, which does not have such a facility.

The second option is a coronagraphic mask that can be positioned in the aberrated HST focal plane, together with a Lyot stop that is simultaneously positioned immediately in front of the M2 mirror, and thus close to the pupil image. All HRC filters, polarimeters, and the prism can be used with the coronagraph.

The coronagraphic mask consists of two circular stops. One is positioned near the circle of least confusion in the center of the aberrated HRC field of view and has a radius of $0.9''$. The second, which is positioned directly over the Fastie spot, is designed for the brightest targets and has a radius of $1.8''$. The masks are positioned in such a way that the central wavelength in the linear ramp filters for each is the same, so observations with both can be made without repositioning the filter wheel. The Lyot stop has the effect of removing the diffracted light halo that surrounds the target, giving almost an order of magnitude higher contrast improvement at the longest wavelengths. The coronagraphic spots will reduce the diffracted light from stellar sources by a factor of ~ 3 at 450 nm. At radii $\geq 3''$ the diffracted light is reduced by a factor of ~ 10 relative to WFPC2. The performance expected from the coronagraph at 450 nm, kindly provided by John Krist and Chris Burrows, is shown in Figure 18.

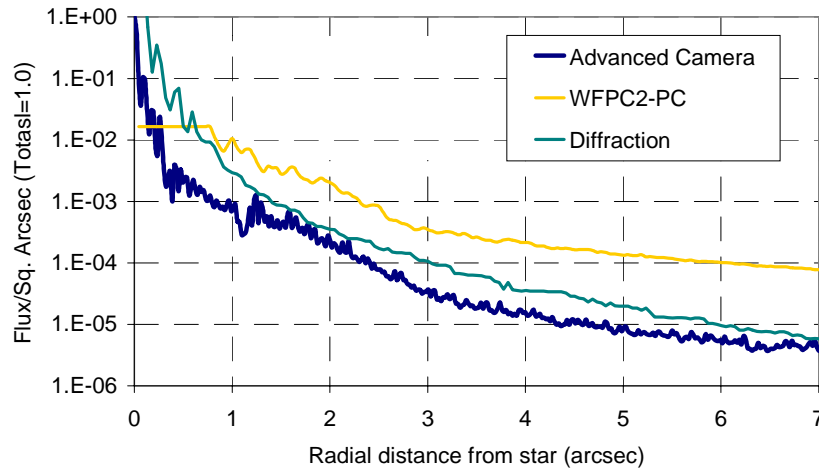


Fig. 18: The expected performance of the Aberrated Beam Coronagraph at 450 nm. The measured WFPC2 point-spread-function is shown for comparison.

8. THE ACS SCIENCE PROGRAM

The ACS Instrument Definition Team plans to use ~ 300 orbits for a WFC survey to investigate the evolution of galaxies and clusters of galaxies at redshifts between $z = 0.2$ and $z = 2.0$. Approximately ten clusters will be chosen at redshifts between 0.5 and 1.0 for a deep two-color survey. The goal of this program is to establish the evolution of the cluster galaxies and the evolution of structure in the parent clusters from $z = 1.0$ to $z = 0.5$. Our cluster sample will be chosen to span the likely range of cluster types. We will determine the role of mergers in producing S0 and cD galaxies, and investigate the evolution of AGNs within the clusters. We plan to use lensed galaxies to study faint field galaxies at higher redshifts.

We will take deep images of two known lensing clusters at $z = 0.2$ to 0.4 and use the morphologies and distribution of lensed galaxies to measure the distribution of dark matter in the clusters' halos. Figure 19 is a simulated ACS image of a lensing cluster at $z = 0.4$, kindly provided by Dr. Tom Broadhurst. The simulation uses the method of Bouwens, Broadhurst, and Silk (1998). The image is the superposition of five orbits in each of the ACS Sloan filters g, r, and z. The large number of faint arcs and arclets shows the power of ACS for such studies.

In addition to surveys of known clusters, we plan to survey five fields in strips centered on radio galaxies at $z \sim 2$. The images will be used to look for clusters or proto-clusters around the radio galaxies, and to look for galaxies at $z > 4$. We plan to use a combination of spectra taken with 8-m and 10-m telescopes and colors to measure the redshifts of the faint galaxies.

The IDT will devote ~ 100 orbits to the study of active galactic nuclei. We will use surveys for nuclear disks (Ford *et al.* 1997) and follow-up STIS spectra to study the demographics of massive black holes in an unbiased sample of early type galaxies. The coronagraph will be used to image the host galaxies of luminous quasars and BL LACs out to a redshift of 0.5. We plan to use the low instrumental polarization and high sensitivities of the WFC and HRC for polarimetric observations of jets and active nuclei.

Sparks (1997) has proposed a novel way to measure geometric distances to galaxies. He has shown that polarimetric observations of supernova light echoes can be used to isolate scattering of the supernova flash by dust that is in a plane perpendicular to the line-of-sight. If the epoch of the supernova is known, the angular size of the light echo in the plane of the sky immediately gives a geometric distance. If the epoch is not known, the light echo's angular rate of expansion, as measured from two epochs, gives the distance. We plan to use the high resolution of the HRC to survey for light echoes in late-type galaxies that have HST Cepheid distances.

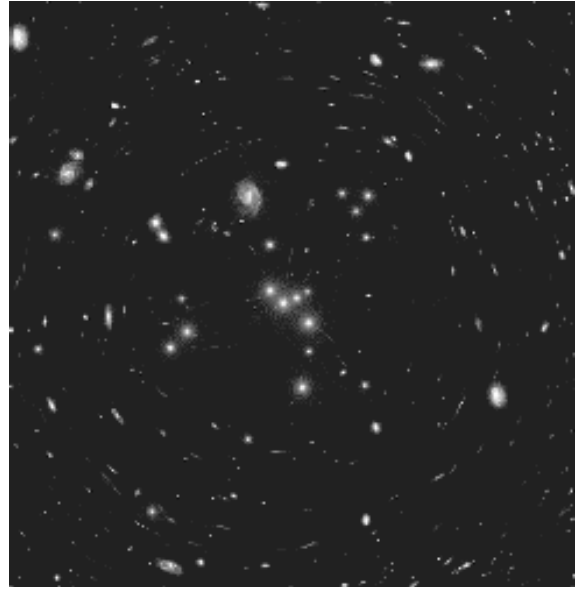


Fig. 19: A simulated ACS image of a lensing cluster of galaxies at $z = 0.4$. The image is a cosmologically and instrumentally realistic superposition of 5 orbits in each of the ACS Sloan filters g, r, and z.

At least 80 orbits will be used for planetary and stellar programs. We will search for planets three ways. First, we will take coronagraphic images of Alpha Cen A and B to look for Jovian-type planets. Our simulations show that detection of planets in the Alpha Cen system will be difficult, but not impossible. The primary limitation will be set by the "breathing" of the HST OTA. This causes the point spread function to vary throughout an orbit, thereby compounding the problem of distinguishing between a faint planet and an artifact in the diffraction pattern. Our second approach will be to make an astrometric and photometric search for planets around the brown dwarf GL 229 B (Nakajima *et al.* 1995; Golimowski *et al.* 1998) Because this "failed star" is only 50 times more massive than Jupiter, at a given separation it will have a larger reflex motion from the gravitation pull of a Jovian-mass planet than any other known star. Because GL 229B is little larger than Jupiter, there is an appreciable probability of detecting partial eclipses from planets as small as the earth. We will also use the coronagraph to search for Beta Pictoris-type proto-planetary disks (Golimowski *et al.*, 1993; Paresce and Burrows, 1996; Heap *et al.* 1998) around nearby stars. Warps in the disks can be used to look for the gravitational signature of planets.

Finally, we will use the SBC to study the temporal and morphological development of the Jovian and Saturnian auroras.

9. ACKNOWLEDGEMENTS

This work is supported by NASA contract NAS5-32865 to the Johns Hopkins University. Ford thanks S. Busching for her perseverance in production of this manuscript.

10. REFERENCES

1. Baum, S., Clampin, M., Hartig, G., Hodge, P., Hulbert, S., Keener, S., Kinney, A., Luther, C., and Sahu, K. 1996, "Space Telescope Imaging Spectrograph Instrument Handbook, Version 1 (Baltimore: STScI).
2. Boucarut, R.A. and Leviton, D.B. 1998, "Broadband Interferometer for Measuring Transmitted Wavefronts of Optical Bandpass Filters for the HST Advanced Camera for Surveys," these proceedings.
2. Bouwens, R.J., Broadhurst, T.J., and Silk, J. 1998, ApJ, in press.
3. Burrows, C. 1990, Optical Telescope Alignment Handbook, Version 1 (Baltimore: STScI).

4. Burrows, C.J., Baggett, S.M., Biretta, J., Casterano, S., Clampin, M., Griffiths, R.E., and Krist, J. 1995, Hubble Space Telescope Wide Field and Planetary Camera 2, Version 3.0 (Baltimore: STScI).
5. Clampin, M., the ACS Science Team, Burmester, B. and Blouke, M., Sirianni, M., 1998, "CCD Detectors for the HST Advanced Camera for Surveys" these proceedings.
6. Fike, S., Schoeneweis, T. 1998, "Flight Software Test and Integration Approach for the HST Advanced Camera for Surveys," these proceedings.
7. Ford, H.C., and the ACS Science Team, 1996, "The Advanced Camera for the Hubble Space Telescope," SPIE, 2807, 184.
8. Ford, H.C., Tsvetanov, Z., Ferrarese, L., Kriss, G., Jaffe, W., Harms, R., and Dressel, L. 1997, "Gaseous Disks in the Nuclei of Elliptical Galaxies" in *Accretion Phenomena and Related Outflows*, IAU colloquium 163, ed. D. T. Wickramasinghe, G.V. Bicknell, and L. Ferrario (ASP Conference Series).
9. Golimowski, D.A., Burrows, C.J., Kulkarni, S.R., Oppenheimer, B.R., and Brukardt, R.A. 1998, "WFPC2 Observations of Gliese 229B: Optical Colors and Orbital Motion," *AJ*, in press.
10. Golimowski, D.A., Durrance, S.T., and Clampin, M. 1993, "Coronagraphic Imaging of the Beta Pictoris Circumstellar Disk: Evidence of Changing Disk Structure at 100 AU," *ApJ*, 411, L41.
11. Hartig, G.F., Ford, H.C., Sullivan, J.F., Gracey, R., Johnson, E., Bartko, F., and Clampin, M. 1998, "Optical Performance Verification and Calibration of the HST Advanced Camera for Surveys," these proceedings.
12. Heap, S.R., Brown, T.M., Hubeny, I., Landsman, W., Yi, S., Fanelli, M., Gardner, J.P., Lanz, T. Maran, S.P., Sweigart, A., Kaiser, M.E., Linsky, J., Timothy, J.G., Lindler, D., Beck, T., Bohlin, R.C., Clampin, M., Grady, J., Loiacono, J., and Krebs, C. 1998, "Ultraviolet Spectral Dating of Stars and Galaxies," *ApJ*, 492, L131.
13. Johnson, G. 1998, "Thermal Management for CCD Performance on the Advanced Camera for Surveys." these proceedings.
14. Krebs, C., LaJeunesse, T., and Ford, H.C. 1998, "Program Management of the HST Advanced Camera for Surveys: A New Approach," these proceedings.
15. Leviton, D.B., Tsvetanov, Z., Woodruff, R., and Mooney, T.A. 1998, "Design and Specification of Optical Bandpass Filters for the HST Advanced Camera for Surveys," these proceedings.
16. Leviton, D.B., Boucarut, R.A., Content, D.A., Miner, L.A., Norton, T.A., Petrone, P., Bush, F.D., Puc, B., Standley, C. and Tsvetanov, Z. 1998, "Optical Metrology for the Filter Set for the HST Advanced Camera for Surveys," these proceedings.
17. Nakajima, T., Oppenheimer, B. R., Kulkarni, S. R., Golimowski, D. A., Matthews, K., and Durrance, S. T. 1995, *Nature*, 378, 463.
18. Paresce, F., and Burrows, C. 1987, "Broad-band Imaging of the Beta Pictoris Circumstellar Disk," *ApJ*, 319, L23.
19. Postman, M. and the ACS Science Team 1998, "The Science Program of the HST Advanced Camera for Surveys," these proceedings.
20. Rafal, M., Johnson, G., Schweickart, R.B., Buchko, M., and McIntosh, R. 1998, "Thermal Design for the Advanced Camera for Surveys," these proceedings.
21. Schweickart, R.B., Johnson, G., Buchko, M. 1998, "Flexible Heat Pipes for CCD Cooling on the Advance Camera for Surveys," these proceedings.
22. Sparks, W. 1997, "Geometric Distance Measurements from Supernovae Light Echoes," Cambridge Univ. Press, in press.
23. Tsvetanov, Z.T., Leviton, D. and selected ACS Science Team Members, 1998, "Spectral Optical Elements for the HST Advanced Camera for Surveys," these proceedings.
24. White, R.L., and Becker, I. 1998, "On-board Image Compression for the HST Advanced Camera for Surveys," these proceedings.
25. Woodruff, R.A., and Cahill, R.F. 1998, "Optical Design of the Advanced Camera for Surveys, a Third Generation HST Axial Science Instrument," these proceedings.